DOI 10.1098/rsta.2019.0105

Modelling strain localization in Ti-6Al-4V at high loading rate: A phenomenological approach

Rongxin Zhou [a], Ka Ho Pang [a], Anuj Bisht [a], Anish Roy [a]*, Satyam Suwas [b], Vadim V. Silberschmidt [a]

[a] *Wolfson School of Mechanical, Electrical and Manufacturing Engineering, Loughborough University, LE11 3TU, United Kingdom*

[b] *Department of Materials Engineering, Indian Institute of Science, Bangalore,560012, India*

Abstract

A phenomenological approach based on a combination of a damage mechanism and a crystal-plasticity model is proposed to model a process of stain localization in Ti-6AI-4V at a high strain rate of 10^3 s^{-1}. The proposed model is first calibrated employing a 3D representative volume element model. The calibrated parameters are then employed to investigate the process of onset of strain localization in the studied material. A suitable mesh size is chosen for the proposed model by implementing a mesh-sensitivity study. The influence of boundary conditions on the initiation of the strain localization is also studied. A variation of crystallographic orientation in the studied material after the deformation process is characterized, based on results for different boundary conditions. The study reveals that the boundary conditions significantly influence the formation of shear bands as well as the variation of crystallographic orientation in the studied material. Results also indicate that the onset of strain localization can affect considerably the material's behaviour.

Keywords: Ti-6AI-4V; localization; crystal plasticity; finite-element analysis

DOI 10.1098/rsta.2019.0105

1. Introduction

Titanium alloys are widely used in high-performance applications thanks to their high specific strength. Among titanium alloys, the largest market share is owned by Ti-6Al-4V (Ti64), with applications including sporting goods, biomedical devices and aerospace parts [1,2]. As a result of its prevalence across a wide range of applications, Ti64 was extensively studied over the years. A typical Ti64 alloy consists of a hexagonal close-packed (HCP) α phase and a body-centred cubic (BCC) β phase, generally displaying Widmanstätten α+β colonies [3]. There are numerous studies on the mechanical behaviour of, and microstructural changes in Ti64 alloy and its variants at various temperatures and strain-rate processing regime [4,5]. Multiple experimental studies [4–10] showed that deformation microstructure of Ti-alloy, below their recrystallization temperature, is inherently marked by the presence of regions with localized strain leading to instability with a widespread formation of shear bands. The process of formation of such adiabatic shear bands induces localised softening, which may further promote the generation of voids and cracks [11]. The iniation, evolution and behaviour of these localised instabilities are influenced by the underlying microstructure [5,12]. Wagoner et al. [5] reported that the instabilities (shear band) formed at lower strain values in Ti64 with a Widmanstätten microstructure than in Ti64 with an equiaxed one. Instabilities were observed to form at boundaries of α colonies with 90° misorientation. The addition of boron in small quantities was reported to delay the strain localization and shear-band formation in Ti64 [3,11,12].

A study of strain-localization phenomena is essential as it is a precursor to crack formation and eventual material failure. Most microstructure-based experimental studies dealing with shear-band formation are typically carried out post-failure, and conclusions related to the course of strain-localization events are principally hypothesised. Certainly, a study of the phenomena of strain localization is crucial in developing a predictive capability for analysis of nucleation of instability in the microstructure and material failure. Some attempts at modelling strain localization and shear band phenomenon were reported in the literature [13–17]. Constitutive isotropic material description, employing a modified form of a Johnson-Cook model, is popularly used in such simulations [13,14], which do not account for the underlying anisotropy related to the crystal orientation. It is expected that a change in local material behaviour due to strain localisation will also affect its behaviour in adjacent areas. Surprisingly, this was not investigated in detail in previous studies. This work aims to develop a modelling framework, which captures strain localization with a minimal set of parameters.

The paper is organised as follows: A constitutive description of the crystal-plasticity model is introduced in Section 2. Section 3 presents the details of the suggested computational framework including the finite-element model and calibration of the model parameters. A damage-based mechanism in each slip system was also introduced into the crystal plasticity model to capture the onset of strain localization in Section 3. Numerical simulations of the studied alloy in uniaxial compression are conducted in Section 4 for different boundary conditions with the focus on assessment of strain localization accounting for the boundary-condition effects as well as the influence of strain localization on the adjacent parts of the material. We conclude our study in Section 5.

2. Crystal plasticity theory

In this section, a classical crystal-plasticity (CP) theory adopted in this study is briefly discussed. Here, a deformation gradient, $\mathbf{F}$, can be decomposed into its elastic and plastic parts as,

$$\mathbf{F} = \mathbf{F_e}\mathbf{F_p}, \qquad 2.1$$

where the subscripts '$\mathbf{e}$' and '$\mathbf{p}$' denote the elastic and plastic parts, respectively. By applying the product rule of differentiation, one can obtain the rate of the total deformation gradient, $\dot{\mathbf{F}}$. Therefore, the velocity gradient, $\mathbf{L}$, can be introduced following its definition $\mathbf{L} = \dot{\mathbf{F}}\mathbf{F}^{-1}$ as

$$\mathbf{L} = \dot{\mathbf{F}}_\mathbf{e}\mathbf{F}_\mathbf{e}^{-1} + \mathbf{F}_\mathbf{e}(\dot{\mathbf{F}}_\mathbf{p}\mathbf{F}_\mathbf{p}^{-1})\mathbf{F}_\mathbf{e}^{-1} = \mathbf{L}_\mathbf{e} + \mathbf{L}_\mathbf{p} \,. \tag{2.2}$$

It is assumed that the plastic velocity gradient, $\mathbf{L}_\mathbf{p}$, is induced by shear on each slip system in a crystal. Hence, $\mathbf{L}_\mathbf{p}$ is formulated as the sum of shear rates on all the slip systems, i.e.

$$\mathbf{L}_\mathbf{p} = \sum_{\alpha=1}^{N} \dot{\gamma}^{(\alpha)}\mathbf{s}^{(\alpha)} \otimes \mathbf{m}^{(\alpha)}, \tag{2.3}$$

where $\dot{\gamma}^{(\alpha)}$ is the shear slip rate on the slip system α, N is the total number of slip systems, and unit vectors $\mathbf{s}^{(\alpha)}$ and $\mathbf{m}^{(\alpha)}$ define the slip direction and the normal to the slip plane in the deformed configuration, respectively. Furthermore, the velocity gradient can be expressed in terms of a symmetric rate of stretching, $\mathbf{D}$, and an antisymmetric rate of spin, $\mathbf{W}$, as,

$$\mathbf{L} = \mathbf{D} + \mathbf{W} = (\mathbf{D}_\mathbf{e} + \mathbf{W}_\mathbf{e}) + (\mathbf{D}_\mathbf{p} + \mathbf{W}_\mathbf{p}) = \dot{\mathbf{F}}_\mathbf{e}\mathbf{F}_\mathbf{e}^{-1} + \sum_{\alpha=1}^{N} \dot{\gamma}^{(\alpha)}\mathbf{s}^{(\alpha)} \otimes \mathbf{m}^{(\alpha)}. \tag{2.4}$$

Following the work of Huang [18], a constitutive law is expressed as the relationship between the elastic part of the symmetric rate of stretching, $\mathbf{D}_\mathbf{e}$, and the Jaumann rate of Cauchy stress, $\overset{\nabla}{\boldsymbol{\sigma}}$, i.e.

$$\overset{\nabla}{\boldsymbol{\sigma}} + \boldsymbol{\sigma}(\mathbf{I} : \mathbf{D}_\mathbf{e}) = \mathbf{C} : (\mathbf{D} - \mathbf{D}_\mathbf{p}), \tag{2.5}$$

where $\mathbf{I}$ is the second-order unit tensor, $\mathbf{C}$ is the fourth order, possibly anisotropic, elastic stiffness tensor. The Jaumann stress rate is expressed as

$$\overset{\nabla}{\boldsymbol{\sigma}} = \dot{\boldsymbol{\sigma}} - \mathbf{W}_\mathbf{e}\boldsymbol{\sigma} + \boldsymbol{\sigma}\mathbf{W}_\mathbf{e} \,. \tag{2.6}$$

On each slip system, the resolved shear stress, $\tau^{(\alpha)}$, is expressed by a Schmid law,

$$\tau^{(\alpha)} = \mathbf{sym}(\mathbf{s}^{(\alpha)} \otimes \mathbf{m}^{(\alpha)}) : \boldsymbol{\sigma} \,. \tag{2.7}$$

DOI 10.1098/rsta.2019.0105

The relationship between the shear rate, $\dot{\gamma}^{(\alpha)}$, and the resolved shear stress, $\tau^{(\alpha)}$, on the slip system α is expressed by a power law proposed by Hutchinson [19]:

$$\dot{\gamma}^{(\alpha)} = \dot{\gamma}_0 \left| \frac{\tau^{(\alpha)}}{g^{(\alpha)}} \right|^n \operatorname{sgn}(\tau^{(\alpha)}), \qquad 2.8$$

where $\dot{\gamma}_0$ is the reference shear strain rate, $g^{(\alpha)}$ is the slip resistance and n is the rate-sensitivity parameter. The evolution of $g^{(\alpha)}$ is given by

$$\dot{g}^{(\alpha)} = \sum_{\beta=1}^{N} h_{\alpha\beta} \left| \dot{\gamma}^{(\beta)} \right|, \qquad 2.9$$

where $h_{\alpha\beta}$ is the hardening modulus that can be calculated in the form modified from that proposed by Asaro [20],

$$h_{\alpha\alpha} = h_0 \operatorname{sech}^2 \left[\frac{h_0 \gamma}{\tau_S - \tau_0} \right], \; h_{\alpha\beta} = q h_{\alpha\alpha} (\alpha \neq \beta), \; \gamma = \sum_{\alpha} \int_0^t \left| \dot{\gamma}^{(\alpha)} \right| dt \,. \qquad 2.10$$

Here, h_0 is the initial hardening modulus, q is the latent hardening ratio, τ_0 and τ_S are the shear stresses at the onset of yield and the saturation of hardening, respectively, and γ is the accumulative shear strain over all the slip systems.

3. Computational framework

(a) Finite-element model

Here, the CP model was implemented in general-purpose finite-element software, ABAQUS/Explicit, by employing the user subroutine (VUMAT). Note that the stress update algorithm was based on the Green-Naghdi stress rate in ABAQUS/Explicit environment. Therefore, a conversion algorithm was required to evaluate a stress update based on the Jaumann stress state defined in [21]. A modelling approach based on a 3D representative volume element (RVE) was used to investigate the deformation mechanisms of the studied alloy at room temperature (293 K) with a strain rate of 10^3 s^{-1}. The RVE model (Figure 1(*b*)) have a side length of 200 µm, with 5 grains in each direction, as shown in Figure 1*c* where each cube of a different colour indicates an individual grain. Construction of the RVE model was based on input from experimental data. The inverse pole figure (IPF) of the sample microstructure along the compression direction is shown in Figure 1*a*, plotted using ATEX software [22]. A strong intensity was observed around the (0001) pole in the IPF indicating basal planes oriented along compression direction. The rest of the IPF show random intensity (intensity close to 1). The volume fraction of the basal orientated grains about the compression axis is ~57% as calculated from ATEX. To mimic the experimental condition, the RVE model for simulation was constructed with ~60% of grains with basal orientation and the rest with random orientation. The random orientations were generated via random number functions for Euler angles incorporated in python codes. Figure 1*(b)* represents the crystal orientations of the grains in the model domain, which also show the IPF of the RVE model. Each grain was meshed with 2×2×2 first-order hexahedral reduced-integration elements (C3D8R elements in ABAQUS). A mesh convergence study was performed with a refined mesh where each grain was meshed with 4×4×4 elements which indicate that the chosen mesh is a reasonable balance between computational efficiency and numerical accuracy.

Uniaxial compression deformation was imposed with the use of a velocity constraint applied along the Y-axis as marked in Figure 1*d* with periodic boundary conditions applying on the front and back faces and left and right faces, while the bottom face was constrained in displacement in the Y-direction.

DOI 10.1098/rsta.2019.0105

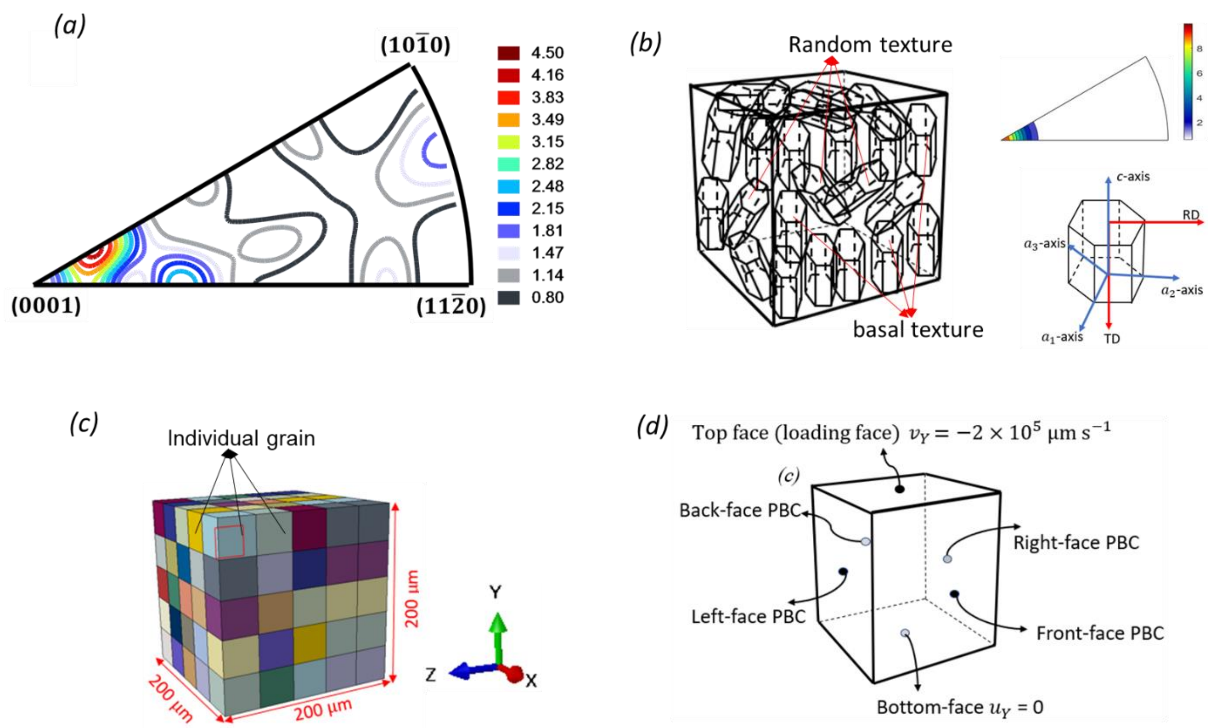

Figure 1.

(a) inverse pole figure of the as-received microstructure ; *(b)* crystal orientation of grains in the RVE (rolling (RD) and transverse (TD) directions); the inverse pole figure shows the numerically modelled texture; *(c)* the RVE model with each colour cube indicating an individual grain; *(d)* imposed boundary conditions.

An HCP crystal orientation is considered for Ti64, with five slip systems active in the material. Here, the basal, prismatic, pyramidal $\langle a \rangle$, and pyramidal $\langle c + a \rangle$ 1st and pyramidal $\langle c + a \rangle$ 2nd slip systems are considered (Table 1), with the corresponding slip planes shown in Figure 2.

Table 1. Slip systems in Ti-6AI-4V

Slip system	Slip plane	Slip direction	Number of modes
Basal	$\{0001\}$	$< 11\bar{2}0 >$	3
Prismatic	$\{10\bar{1}0\}$	$< 11\bar{2}0 >$	3
Pyramidal $\langle \boldsymbol{a} \rangle$	$\{10\bar{1}1\}$	$< 11\bar{2}0 >$	6
Pyramidal $\langle \boldsymbol{c} + \boldsymbol{a} \rangle$ 1st	$\{10\bar{1}1\}$	$< 11\bar{2}3 >$	12
Pyramidal $\langle \boldsymbol{c} + \boldsymbol{a} \rangle$ 2nd	$\{11\bar{2}2\}$	$< 11\bar{2}3 >$	6

DOI 10.1098/rsta.2019.0105

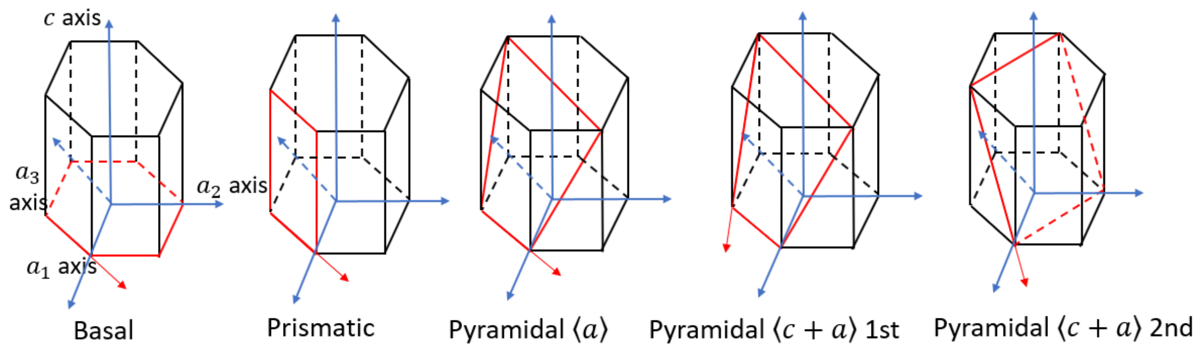

Figure 2.

Slips systems and slip planes in Ti-6AI-4V.

(b) Model verification and parameter calibration

A high strain-rate compression test at a strain rate of 10^3 s^{-1} and room temperature (293 K) was performed using a gas-gun-driven split-Hopkinson pressure bar (SHPB) at Indian Institute of Science Bangalore. For the SHPB test, cylindrical samples were extracted from the as-received hot extruded Ti64 rod with compression axis parallel to the extrusion axis. A cylindrical sample of 3 mm diameter and 3 mm height was used for the test. The stress-strain data for the compression test were extracted from the recorded transmitted and reflected wave signals [8,23,24].

The CP model was calibrated with the experimental SHPB data. As can be seen from Figure 3, a reasonable correlation between the experimental and numerical stress-strain curves for the loading case was achieved after calibration. The parameters related to the elastic constants of the studied alloy are listed in Table 2 while model parameters for the slip deformation modes in the CP model are summarised in Table 3. The reference shear strain rate $\dot{\gamma}_0$ and the rate-sensitivity parameter n were set to be 10^{-3} s^{-1} and 50, respectively. The validity of the parameters should be tested once more experimental results, potentially under complex loading states are available. A modelling approach described in [25] may be attempted once relevant experimental data is available. We leave this as a future work.

DOI 10.1098/rsta.2019.0105

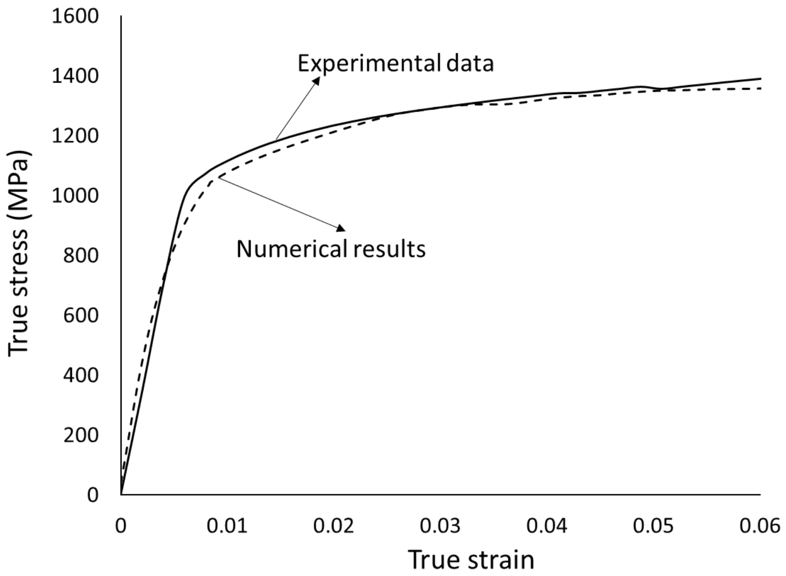

Figure 3.

Model verification with experimental results

Table 2. Elastic constants of Ti-6Al-4V (in GPa)

C_{11}	C_{12}	C_{13}	C_{33}	C_{44}	C_{55}
162.4	92	69	180.7	70.4	49.7

The proposed CP model can be suitably modified to account for effects of temperature and strain rate on the mechanical behaviour of the studied alloy. To accomplish this, the initial critical resolved shear stress, the resistance from grain boundaries and from the interaction of deformation mechanisms, in the hardening law should be defined as a function of temperature and strain rate. In this study, the focus is on the shear-band formation and its effects on material behaviour at high strain rates and room temperature only; thus, the development of temperature- and strain-rate-dependent functions in the hardening law is left for future studies. More details of the theoretical implications are available in [21].

DOI 10.1098/rsta.2019.0105

Table 3. Related parameters (stress in MPa) at reference conditions: T = 293 K, strain rate 10^3 s^{-1}

Slip system	τ_0	τ_s	h_0
Basal	352.3	410	1400
Prismatic	314.3	360	1200
Pyramidal $\langle \boldsymbol{a} \rangle$	428.6	480	1100
Pyramidal $\langle \boldsymbol{c}+\boldsymbol{a} \rangle$ 1st	365	410	4500
Pyramidal $\langle \boldsymbol{c}+\boldsymbol{a} \rangle$ 2nd	423	480	4500

(c) Phenomenological approach for modelling strain localization

To model the initiation of strain localization in the material, a phenomenological damage mechanism was introduced into the CP model. Here, a damage parameter (D) was introduced into the evolution of strength in a slip system, $g^{(\alpha)}$, so that the strength evolution is defined by the following law:

$$\begin{aligned} \dot{g}^{(\alpha)} &= \sum_{\beta=1}^{N} h_{\alpha\beta} \left|\dot{\gamma}^{(\beta)}\right|, \gamma^{(\alpha)} \le \gamma_{cr}^{(\alpha)} \\ \dot{g}^{(\alpha)} &= \sum_{\beta=1}^{N} h_{\alpha\beta} \left|\dot{\gamma}^{(\beta)}\right| - \dot{D}(\gamma), \gamma^{(\alpha)} > \gamma_{cr}^{(\alpha)} \end{aligned}, \quad 3.1$$

where $\gamma_{cr}^{(\alpha)}$ is the critical shear strain at α slip system. We choose $\gamma_{cr}^{(\alpha)} = 0.1$ in this model, which implies that softening is induced once the net strain in a slip system exceeds 0.1. Next, the damage in the material ($\dot{D}(\gamma)$) evolves as

$$\dot{D}(\gamma) = (\tau_s - \tau_0) m \dot{\gamma} e^{-m\dot{\gamma}} \quad 3.2$$

where m is a calibration parameter with a value of 100.

The proposed damage-based softening mechanism in each slip system (Eq.3.2) is phenomenological. The underlying justification for this is that a given slip system can sustain

DOI 10.1098/rsta.2019.0105

a critical amount of deformation slip before incurring damage which will allow for a rapid evolution of plastic slip which lead to strain localization

(d) Mesh-size sensitivity

Numerical analysis incorporating strain localisation is typically mesh-dependent. Thus, a mesh-sensitivity analysis is key in determining the efficacy of such a phenomenological approach. Here, simulations with three different mesh sizes, with a nominal element size, *h*, of 0.15, 0.3 and 0.6 μm were conducted for a specimen with a dimension of $30\ \mu\text{m} \times 30\ \mu\text{m} \times 3\ \mu\text{m}$. The domain was formed by 4 grains as shown in Figure 4*b*. Without any loss of generality, Grain 1 and Grain 4 were assumed to be identical; a similar assumption was made for Grain 2 and Grain 3 as well. The top face of this model was deformed by imposing a velocity boundary control, corresponding to a strain rate of $10^3\ s^{-1}$. A periodic boundary condition (PBC) was applied on the left and right surfaces of the model. The bottom face was constrained in displacement in the Y-direction (Figure 4*a*). Plane-strain conditions were imposed on the front and back faces of the modelled domain.

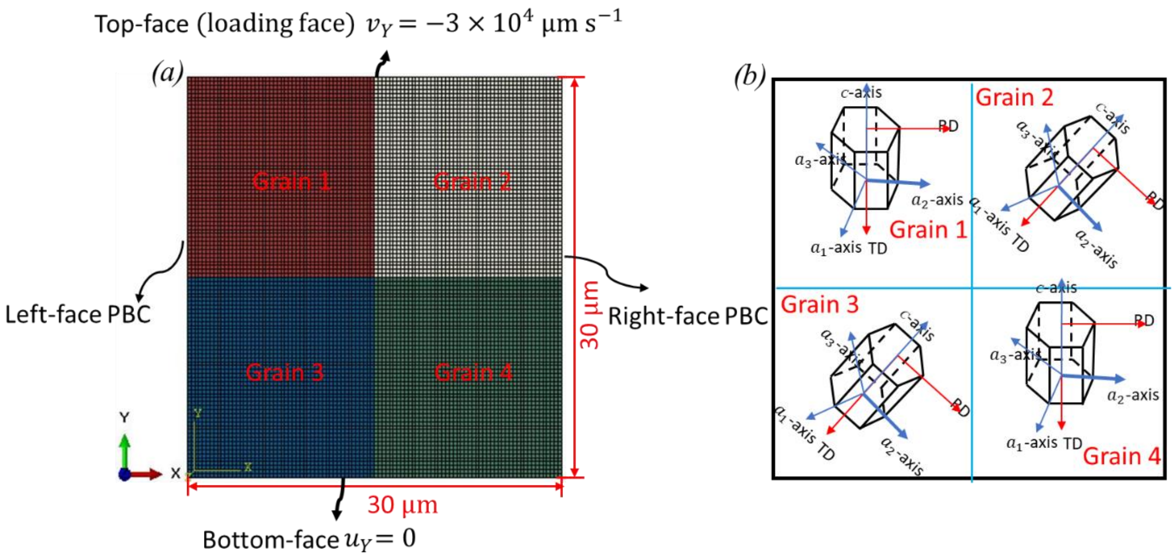

Figure 4.

Simple RVE model for mesh-sensitivity study: *(a)* loading and boundary conditions; *(b)* grain size and orientation in the model domain.

DOI 10.1098/rsta.2019.0105

Due to imposed deformation, strain localisation occurred in the material, represented by the total accumulated shear strain overall slip systems ($\sum|\gamma^{(\alpha)}|$) in every grain. Bands of strain localisation, similar to shear bands are shown in Figure 5*a* for 3 mesh densities. As expected, these bands were better resolved with a finer mesh; however, the overall features were similar and comparable across all the 3 meshes. For further analysis, two diagonal paths were chosen in the meshed domain, indicated by paths A-B and C-D in Figure 5*a* and the total accumulated $\sum|\gamma^{(\alpha)}|$ was traced along these paths in Figure 5*b*, *c*. The results indicate that an element size corresponding to $h = 0.3\,\mu\text{m}$ is reasonable, when compared to the those for the finer mesh. Hence, a mesh size of 0.3 μm was chosen for the investigation of strain localization in the developed crystal-plasticity finite-element model hereinafter.

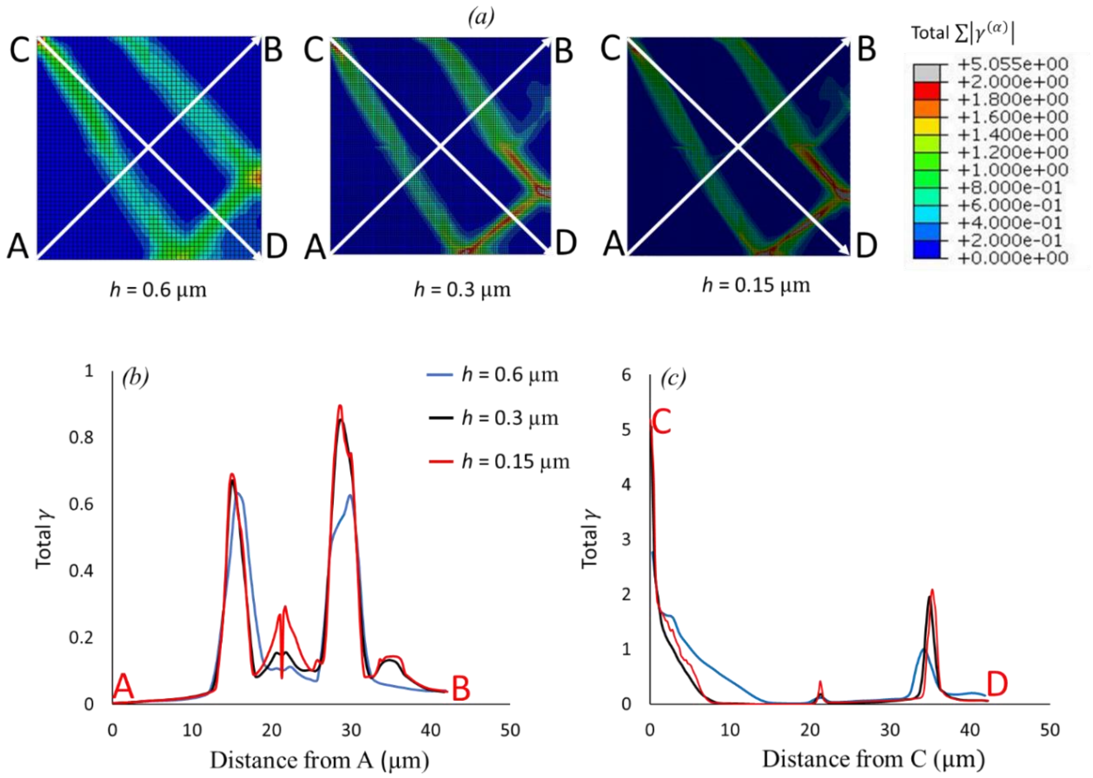

Figure 5.

Mesh-size sensitivity study: *(a)* effect on the pattern of strain localization; *(b)* evolution of accumulated shear strain along path A-B; *(c)* evolution of accumulated shear strain along path C-D.

DOI 10.1098/rsta.2019.0105

(e) Microstructural model

Next, the effect of strain localisation in a representative microstructural ensemble was studied. A Ti64 sample was sectioned to expose the transverse plane. An electron back-scattered diffraction (EBSD) technique was employed to obtain the character of microstructural orientation in the sample. The EBSD data obtained from the scan was further analysed with DREAM.3D, and the reconstruction of the EBSD data was performed with the Abaqus Hexahedron Writer available in the software. An area with a random grain structure with dimensions $30\ \mu\text{m} \times 30\ \mu\text{m} \times 3\ \mu\text{m}$ was selected at the centre of the scanned area (Figure 6). 16 crystallographic orientations were identified in the selected area. A list of the grains with their orientations is presented in Figure 6 and Table 4. The selected area was converted into an RVE model of the Ti64 sample. Steps followed to obtain the FE representation of the microstructure model are shown in Figure 6. Here, due to the inherent limitation of the available EBSD scans, the microstructure at the sample surface was extracted. The in-depth grain morphology data is not available. For this reason, a 2D plane-strain condition with only one grain in the depth direction. is modelled in the current study. The plane-strain state considered in the present study is consistent with the real material state.

Obviously, the grain structure in the depth-direction should influence the macroscopic as well as the local response of the studied alloy. Should a true 3D grain morphology data be made available the proposed modelling approach can capture the nuances of strain localization in the depth direction. The mesh density used was identical to the converged mesh obtained earlier. The boundary conditions imposed on the RVE were identical to those employed in Section 3.4.

DOI 10.1098/rsta.2019.0105

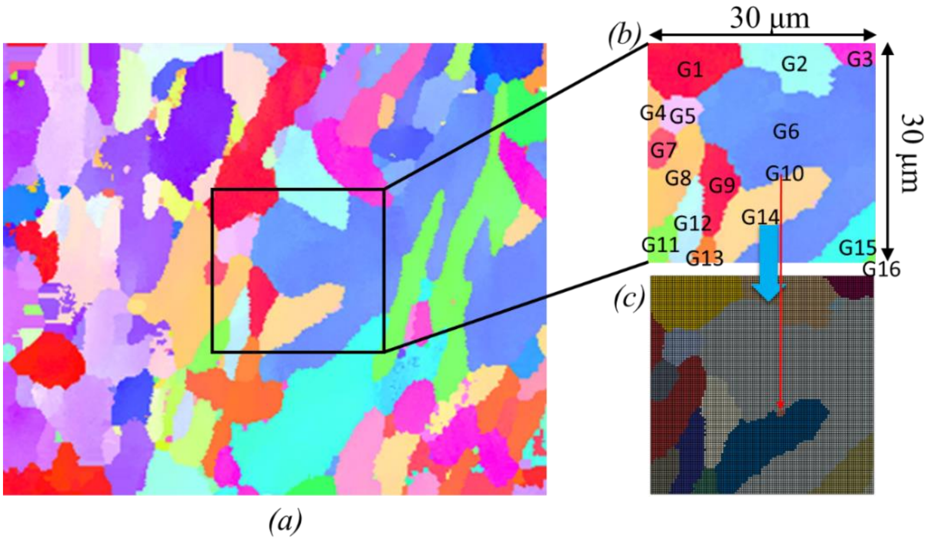

Figure 6.

Generation of the finite-element model. *(a)* microstructure from EBSD data; *(b)* chosen domain for RVE model sgowing the grains identified ranging from G1 through G16; *(c)* FE mesh of the RVE model.

Table 4. Initial crystal orientations with three Euler angles (unit degree) for the identified grains

Grain number	Euler angle $\boldsymbol{\varphi_1}$	Euler angle ∅	Euler angle $\boldsymbol{\varphi_2}$
G1	88.11	155.84	215.52
G2	331.14	69.30	314.12
G3	50.71	11.73	121.03
G4	145.05	131.96	280.51
G5	37.23	42.17	81.29
G6	224.84	79.83	127.18
G7	91.87	155.19	229.36
G8	144.92	131.93	280.70
G9	88.12	155.84	215.53
G10	283.67	92.84	315.59
G11	44.73	101.07	232.04
G12	330.79	69.53	314.26
G13	235.65	138.32	121.35
G14	143.36	126.94	252.79
G15	331.15	70.15	306.29
G16	45.81	100.40	293.00

DOI 10.1098/rsta.2019.0105

4. Results and discussions

(a) Effects of boundary conditions

First, the effects of imposed boundary conditions on the formation of the strain localization were analysed in the studied alloy. Here, two different boundary conditions, namely, the effect of imposing periodic boundary conditions (PBC) and traction-free surface boundary conditions (FRE), are studied in detail. Loading was applied on the top surface with a velocity boundary condition, while the bottom surface is fixed in displacement in the Y-direction (Figure 7).

Strain localisation was significantly influenced by the imposed boundary conditions. The pattern of the strain localization is pronounced, with an imposed periodicity at the left and right surfaces. This boundary condition is typically imposed when the spatial range of a sample in the X-direction is large. In contrast, when traction-free boundaries were assumed, a single dominant shear band was observed in the material volume. This indicates that shear bands are denser in a constrained material domain corresponding to the interior of a bulk crystalline material. By a similar argument, less pronounced localisation and shear- band formation are expected near the free surface of a deformed component. This conclusion is consistent with the experimental observations in [26–30], indicating that the shear band density was higher in central parts of specimens than elsewhere.

DOI 10.1098/rsta.2019.0105

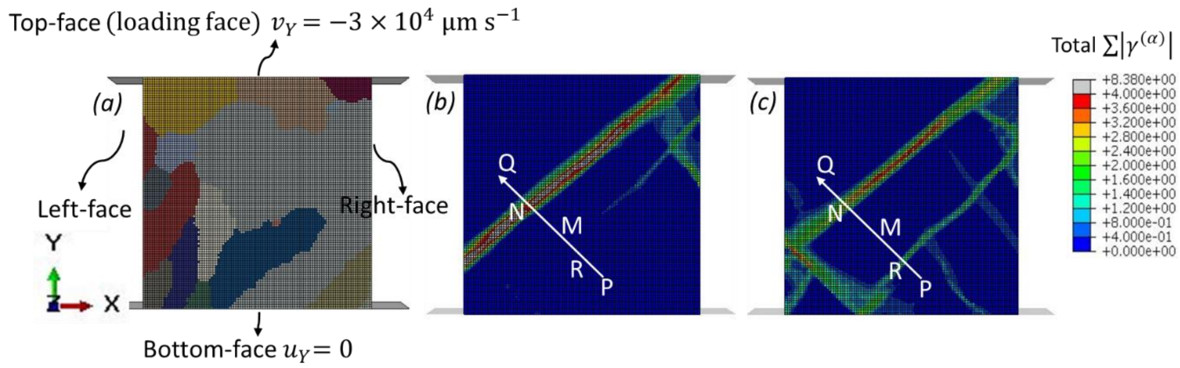

Figure 7.

Effects of boundary conditions on strain localization: *(a)* microstructured model and boundary conditions; *(b)* case with FRE boundary conditions (right and left face are traction- free); *(c)* case with PBC boundary conditions (right and left face are constrained via periodic boundary conditions).

(b) Misorientation angle

To characterize the variation of crystallographic orientation of the studied alloy after the deformation process, the concept of misorientation angle was invoked. This is defined as

$$\theta = \left|\cos^{-1}\left\{\frac{\mathrm{tr}\left(\mathbf{g}_A\mathbf{g}_B^{-1} - 1\right)}{2}\right\}\right|, \qquad 4.1$$

where θ is the misorientation angle, $\mathbf{g}_A$ and $\mathbf{g}_B$ are the orientation matrices at chosen spatial locations A and B, respectively. In this paper, the undeformed crystallographic structure was considered as the reference configuration for calculation of the misorientation angle. The variation of the misorientation angle along the path P-Q (perpendicular to the strain-localization band) is shown in Figure 8. Along the path P-Q, three other points, -R, M and N- were selected (see Figure 7); They respectively represent the regions in the shear band near point P, between two shear bands and near point Q.

DOI 10.1098/rsta.2019.0105

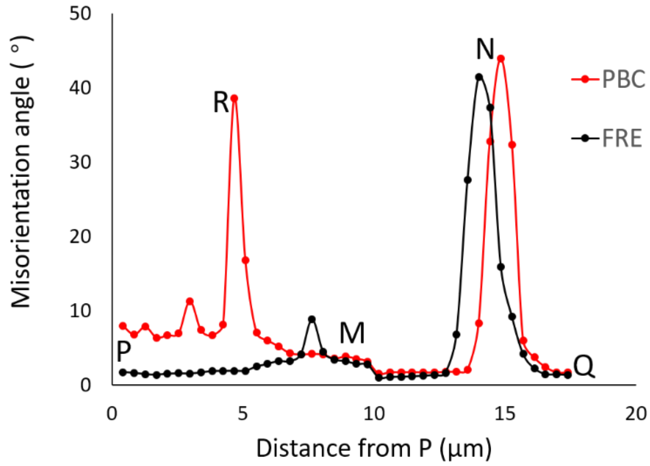

Figure 8.

Misorientation angle along path P-Q across shear bands

The change in the misorientation angle after deformation was compared for the two selected boundary conditions. The character of misorientation angle along the path P-Q varies for the two boundary conditions, with higher values corresponding to the constrained domain. Two obvious peaks for the PBC were observed, while there was only one distinct peak for FRE boundary conditions. This is consistent with the number of shear bands along the path P-Q (Figure 7). This suggests that strain localization can strongly influence the material behaviour in local areas by changing significantly the crystal orientation post-deformation.

5. Concluding Remarks

A crystal-plasticity finite-element modelling approach for the formation of the strain localization in Ti-6AI-4V was presented, incorporating a strain-softening/damage description for each slip system. The parameters of the crystal plasticity model were calibrated against the experimental studies in terms of the stress-strain curve at room temperature and high strain strain rate of 10^3 s^{-1}. The model is shown to have the ability to capture the formation of the strain localization in the studied alloy. The effect of boundary conditions on strain localization was analysed. The study revealed that boundary conditions significantly influenced the formation process of strain localization including the pattern and the number of shear bands formed. Additionally, it was demonstrated that strain localisation can affect the local mechanical response of Ti64 as a result of a change in the misorientation angle of the polycrystalline ensemble. It was observed that the magnitude of the misorientation angle was higher in the interior parts of the specimen than near its free surfaces.

Acknowledgement

Funding from the Engineering and Physical Sciences Research Council (UK) through grant EP/P027555/1, project H^2 Manufacturing, is gratefully acknowledged.

References

1. Williams JC, Starke EA. 2003 Progress in structural materials for aerospace systems. *Acta Mater.* **51**, 5775–5799. (doi:10.1016/j.actamat.2003.08.023)
2. Niinomi M. 2003 Recent research and development in titanium alloys for biomedical applications and healthcare goods. *Sci. Technol. Adv. Mater.* **4**, 445–454. (doi:10.1016/J.STAM.2003.09.002)
3. Roy S, Sarkar A, Suwas S. 2010 On characterization of deformation microstructure in Boron modified Ti–6Al–4V alloy. *Mater. Sci. Eng. A* **528**, 449–458. (doi:10.1016/J.MSEA.2010.09.026)
4. Roy S, Suwas S. 2013 The influence of temperature and strain rate on the deformation response and microstructural evolution during hot compression of a titanium alloy Ti–6Al–4V–0.1B. *J. Alloys Compd.* **548**, 110–125. (doi:10.1016/J.JALLCOM.2012.08.123)
5. Wagoner Johnson AJ, Bull CW, Kumar KS, Briant CL. 2003 The influence of microstructure and strain rate on the compressive deformation behavior of Ti-6Al-4V. *Metall. Mater. Trans. A* **34**, 295–306. (doi:10.1007/s11661-003-0331-6)
6. Kailas S V., Prasad YVRK, Biswas SK. 1994 Flow Instabilities and fracture in Ti-6Al-4V deformed in compression at 298 K to 673 K. *Metall. Mater. Trans. A* **25**, 2173–2179.

(doi:10.1007/BF02652318)

7. Semiatin SL, Seetharaman V, Ghosh AK. 1999 Plastic flow, microstructure evolution, and defect formation during primary hot working of titanium and titanium aluminide alloys with lamellar colony microstructures. *Philos. Trans. R. Soc. London. Ser. A Math. Phys. Eng. Sci.* **357**, 1487–1512. (doi:10.1098/rsta.1999.0386)

8. Hazell PJ, Appleby-Thomas GJ, Wielewski E, Escobedo JP. 2014 The shock and spall response of three industrially important hexagonal close-packed metals: magnesium, titanium and zirconium. *Philos. Trans. R. Soc. A Math. Phys. Eng. Sci.* **372**, 20130204–20130204. (doi:10.1098/rsta.2013.0204)

9. Bieler TR, Crimp MA, Yang Y, Wang L, Eisenlohr P, Mason DE, Liu W, Ice GE. 2009 Strain heterogeneity and damage nucleation at grain boundaries during monotonic deformation in commercial purity titanium. *JOM* **61**, 45–52. (doi:10.1007/s11837-009-0180-x)

10. Bieler T, Goetz RL, Semiatin SL. 2005 Anisotropic plasticity and cavity growth during upset forging of Ti–6Al–4V. *Mater. Sci. Eng. A* **405**, 201–213. (doi:10.1016/J.MSEA.2005.05.064)

11. Roy S, Suwas S. 2014 On the absence of shear cracking and grain boundary cavitation in secondary tensile regions of Ti–6Al–4V–0.1B alloy during hot (α + β)-compression. *Philos. Mag.* **94**, 447–463. (doi:10.1080/14786435.2013.855334)

12. Roy S, Suwas S, Tamirisakandala S, Srinivasan R, Miracle DB. 2012 Microstructure and texture evolution during β extrusion of boron modified Ti–6Al–4V alloy. *Mater. Sci. Eng. A* **540**, 152–163. (doi:10.1016/J.MSEA.2012.01.120)

13. Calamaz M, Coupard D, Nouari M, Girot F. 2011 Numerical analysis of chip formation and shear localisation processes in machining the Ti-6Al-4V titanium alloy. *Int. J. Adv. Manuf. Technol.* **52**, 887–895. (doi:10.1007/s00170-010-2789-x)

14. Ye GG, Xue SF, Jiang MQ, Tong XH, Dai LH. 2013 Modeling periodic adiabatic shear band evolution during high speed machining Ti-6Al-4V alloy. *Int. J. Plast.* **40**, 39–55. (doi:10.1016/J.IJPLAS.2012.07.001)

15. Liu Q, Roy A, Tamura S, Matsumura T, Silberschmidt V V. 2016 Micro-cutting of single-crystal metal: Finite-element analysis of deformation and material removal. *Int. J. Mech. Sci.* **118**, 135–143. (doi:10.1016/J.IJMECSCI.2016.09.021)

16. Hunt GW, Dodwell TJ, Hammond J. 2013 On the nucleation and growth of kink and shear bands. *Philos. Trans. R. Soc. A Math. Phys. Eng. Sci.* **371**, 20120431–20120431. (doi:10.1098/rsta.2012.0431)

17. Benzi R, Sbragaglia M, Bernaschi M, Succi S. 2011 Shear banding from lattice kinetic models with competing interactions. *Philos. Trans. R. Soc. A Math. Phys. Eng. Sci.* **369**, 2439–2447. (doi:10.1098/rsta.2011.0058)
18. Huang Y. 1991 A User-material subroutine incorporating single crystal plasticity in the ABAQUS finite element program. Mech report 178, Division of Engineering and Applied Sciences, Harvard University.
19. Hutchinson JW. 1976 Bounds and Self-Consistent Estimates for Creep of Polycrystalline Materials. *Proc. R. Soc. A Math. Phys. Eng. Sci.* **348**, 101–127. (doi:10.1098/rspa.1976.0027)
20. Asaro RJ. 1983 Crystal Plasticity. *J. Appl. Mech.* **50**, 921. (doi:10.1115/1.3167205)
21. Liu Q, Roy A, Silberschmidt V V. 2017 Temperature-dependent crystal-plasticity model for magnesium: A bottom-up approach. *Mech. Mater.* **113**, 44–56. (doi:10.1016/J.MECHMAT.2017.07.008)
22. Beausir B, Fundenberger J-J. 2017 Analysis Tools for Electron and X-ray diffraction, ATEX - software. (doi:www.atex-software.eu)
23. Yang R, Zhang H, Shen L, Xu Y, Bai Y, Dodd B. 2014 A modified split Hopkinson torsional bar system for correlated study of τ-γ relations, shear localization and microstructural evolution. *Philos. Trans. A. Math. Phys. Eng. Sci.* **372**, 20130208. (doi:10.1098/rsta.2013.0208)
24. Lindholm US. 1964 Some experiments with the split hopkinson pressure bar∗. *J. Mech. Phys. Solids* **12**, 317–335. (doi:10.1016/0022-5096(64)90028-6)
25. Liu Q, Roy A, Silberschmidt V V. 2016 Size-dependent crystal plasticity: From micro-pillar compression to bending. *Mech. Mater.* **100**, 31–40. (doi:10.1016/J.MECHMAT.2016.06.002)
26. Timothy SP, Hutchings IM. 1985 Initiation and growth of microfractures along adiabatic shear bands in Ti–6AI–4V. *Mater. Sci. Technol.* **1**, 526–530. (doi:10.1179/mst.1985.1.7.526)
27. Tvergaard V, Needleman A. 1993 Shear Band Development in Polycrystals. *Proc. R. Soc. A Math. Phys. Eng. Sci.* **443**, 547–562. (doi:10.1098/rspa.1993.0161)
28. Liao S, Duffy J. 1998 Adiabatic shear bands in a TI-6Al-4V titanium alloy. *J. Mech. Phys. Solids* **46**, 2201–2231. (doi:10.1016/S0022-5096(98)00044-1)
29. Zhang Z, Eakins DE, Dunne FPE. 2016 On the formation of adiabatic shear bands in textured HCP polycrystals. *Int. J. Plast.* **79**, 196–216. (doi:10.1016/J.IJPLAS.2015.12.004)

30. Lunt D, Xu X, Busolo T, Quinta da Fonseca J, Preuss M. 2018 Quantification of strain localisation in a bimodal two-phase titanium alloy. *Scr. Mater.* **145**, 45–49. (doi:10.1016/J.SCRIPTAMAT.2017.10.012)